Journal of Materials Chemistry A

Enhancing the performance of MnO by double carbon modification for advanced lithium-ion battery anode

Journal:	*Journal of Materials Chemistry A*
Manuscript ID	TA-ART-08-2015-006095.R2
Article Type:	Paper
Date Submitted by the Author:	20-Nov-2015

Complete List of Authors:	Jiang, Xiaojian; Xiamen Products Quality Supervision & Inspection Institute, Yu, Wei; Center for Advanced Energy Materials & Technology Research (AEMT), and School of Chemistry and Chemical Engineering, Shandong University, Jinan 250100, P.R. China, Wang, Hui; Enviromental Protection Administration of Linyi, Xu, Huayun; Shandong University, Key Laboratory of Colloid and Interface Chemistry Liu, Xizheng; Tianjin University of Technology, ; AIST, Ding, Yi; Tianjin University of Technology,

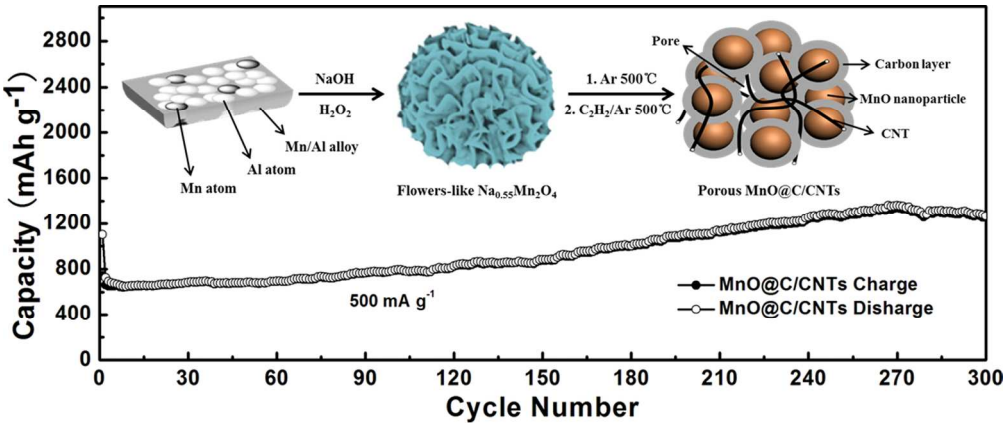

Unique porous MnO with micro/nano architectures have been in-situ decorated by carbon layers on the surface and carbon nanotubes doping. The composites exhibit stable electrochemical performance as anode for Li ion battery.
199x83mm (300 x 300 DPI)

Journal Name

ARTICLE

Enhancing the performance of MnO by double carbon modification for advanced lithium-ion battery anode

Received 00th January 20xx,
Accepted 00th January 20xx

DOI: 10.1039/x0xx00000x

www.rsc.org/

Xiaojian Jiang,[b] Wei Yu,[c] Hui Wang,[d] Huayun Xu,[c] Xizheng Liu,[a*] and Yi Ding[a*]

Porous hybrid materials with designed micro/nano sub-structures have been recognized as promising anodes for lithium-ion batteries (LIBs) due to the high capacity and reliable performance. The low electric conductivity and side-reactions at the interface of electrode/electrolyte prohibit its practical applications. Carbon materials modification can effectively enhance the conductivity and mechanical property, and suppress the direct contact between electrode and electrolyte, leading to enhanced performance. Herein, unique porous MnO with micro/nano architectures have been in-situ decorated by carbon layers on the surface and carbon nanotubes doping between the particles (denoted as MnO@C/CNTs) by a catalytic chemical vapor deposition (CCVD) treatment. As anodes in LIBs, these MnO@C/CNTs exhibit remarkable cycling performance (1266 mAh g^{-1} after 300 cycles at 500 mA g^{-1}), and good rate capability (850 mAh g^{-1} after 100 cycles at 100 mA g^{-1}). The inspiring performance is associated with the carbon modified porous micro/nano structure features which can buffer the volume expansion and promote the ion/electron transfer at the interface of electrode/electrolyte.

Introduction

Lithium-ion batteries (LIBs) have gained great success in portable devices during the past two decades because of their high capacity and cycle stability.[1-3] The ever-increasing market of electric vehicles and smart grid requires the improvement of electrochemical performance in capacity, cycle life, rate capability in LIBs.[4-6] As attractive candidate anode materials, transition metal oxides function through a redox conversion reaction mechanism and therefore can exhibit higher theoretical specific capacity than carbon-based materials (graphite, 372 mAh g^{-1} for LiC_6).[7] Among them, MnO based materials are extremely favored due to their high theoretical capacity ($MnO + 2\ Li^+ + 2\ e^- \leftrightarrow Li_2O + Mn$, 756 mAh g^{-1}), relatively low voltage hysteresis (1.032 V *vs.* Li^+/Li), natural abundance, low cost and environmental friendliness.[8] However, the drastic volume change during discharge/charge process, leading to performance fading, prohibits their practical applications.[9] With this respect, porous architectures with designed micro/nano sub-structures are highly desired in improving the capacity retention and power densities.[10, 11] We have also fabricated porous MnO_x anode with a specific capacity of 757 mAh g^{-1} at 500 mA g^{-1} after 100 cycles by a facile dealloying method.[12] However, the rate performance cyclability are still unsatisfactory due to the intrinsically low electronic conductivity, similar to other transition metal oxides.[2]

Addressing these issues, combination of carbon modification with nanotechnology seems to be an effective way.[13] The electrode materials at nano-scale usually suffer from agglomeration and side reactions with electrolyte, resulting the poor coulombic efficiency and unstable electrode/electrolyte interface.[14, 15] Improvements of modified nano-scale oxide anodes by carbon materials can be expected as: prohibiting the nano-particles aggregation, buffering the volume expansion, enhancing the electrical conductivity as well as promoting the ion transfer at the interface of electrode/electrolyte.[16-18] Many approaches have been reported to enhance the electrochemical performance of MnO by carbon materials. For example, MnO@C core-shell nanowires (801 mAh g^{-1} at 500 mA g^{-1} after 200 cycles),[19] nanorods (600 mAh g^{-1} at 200 mA g^{-1} after 40 cycles),[20] MnO/Graphene (930 mAh g^{-1} at 500 mA g^{-1} after 470 cycles)[21] and MnO/MWNTs (597 mAh g^{-1} at 130 mA g^{-1} after 200 cycles[22] have been intensively studied. The improved electrochemical performances have been achieved due to either surface coating or doping between MnO particles by carbon materials.

In present work, we develop a new approach to modify the microsphere MnO materials by a surface carbon layer coating and carbon nanotubes doping among the MnO microspheres by a CCVD technique.[23, 24] To the best of our knowledge, this is the first report about anode modification by two different carbon materials simultaneously. As an anode of LIBs, the resultant MnO@C/CNTs

[a] *Institute for New Energy Materials and Low-Carbon Technologies, and School of Materials Science and Engineering, Tianjin University of Technology, Tianjin 300384, P.R. China E-mail: xzliu@tjut.edu.cn, yding@tjut.edu.cn.*
[b] *Xiamen Products Quality Supervision & Inspection Institute, Xiamen 361004, P.R. China*
[c] *Center for Advanced Energy Materials & Technology Research (AEMT), and School of Chemistry and Chemical Engineering, Shandong University, Jinan 250100, P.R. China*
[d] *Environmental Protection Administration of Linyi, Linyi Shandong 276000, P.R. China*

† Electronic Supplementary Information (ESI) available: The nitrogen adsorption-desorption isotherms, SEM image and XPS of porous MnO@C/CNTs. TEM image and XRD pattern of MnO/CNTs. Nyquist plots of porous MnO@C/CNTs electrodes charged to 3 V after different discharge/charge cycles at 500 mA g^{-1}. Table of comparison of cycling performances of MnO-based anode materials.
See DOI: 10.1039/x0xx00000x

material exhibits distinct features: the porous microsphere MnO structure can buffer the repeated volume expansion during cycles, the surface carbon coating layer can not only promote the conductivity, preserve the microsphere morphology of MnO during discharge/charge process, but also alleviate the formation/decomposition of solid electrolyte interphase (SEI) layer, the CNTs doping between the particles can further improve the conductivity of the electrode. Benefiting from these unique structural characteristics, this hybrid material exhibits superior cycling performance and rate capability as an anode for LIBs.

Experimental

Synthesis of flowers-like $Na_{0.55}Mn_2O_4$

The flowers-like precursors were synthesized according to previous description.[12] Firstly, Mn/Al alloys were fabricated by melting from high purity Mn (99.9 wt.%) and Al (99.9 wt.%) in 5:95 atomic ratio. Secondly, the alloys with appropriate size were re-melted and spinning into thin foils with thickness of about 50 μm. Next, 0.2 g foils were located into 72 mL H_2O and 28 mL H_2O_2 (30 wt.%) in a flask under vigorously stirring. Subsequently, 100 mL NaOH (2 mol L^{-1}) was dropped at a rate of 10 mL min^{-1}, and kept for 8 h. The obtained precursors were washed with ultra-pure water and dried in vacuum oven at 60°C.

Synthesis of porous MnO@C/CNTs

Porous MnO@C/CNTs was synthesized by calcining the flowers-like $Na_{0.55}Mn_2O_4$ at 500°C for 30 min in Ar, followed by 60 min in C_2H_2/Ar atmosphere at a flow rate of 30 mL min^{-1}. Then, the product was washed several times with ultra-pure water and dried in vacuum oven. For comparing and revealing the formation process, flowers-like $Na_{0.55}Mn_2O_4$ were calcined at 500°C for 30 min in Ar atmosphere, at an increasing rate of 5°C min^{-1}. Meanwhile, porous MnO/CNTs (without ultra-thin overlayers) material was obtained by calcining the flowers-like $Na_{0.55}Mn_2O_4$ at 500°C for 60 min in C_2H_2/Ar atmosphere at a flow rate of 30 mL min^{-1} only without pretreatment. When $Na_{0.55}Mn_2O_4$ was decomposed into MnO@C/CNTs after thermal treatment, the sodium hydroxide produced was washed by ultra-pure water, and the supernate is alkaline, as shown in Fig. S1. After 3 times centrifugation, the supernate is neutral.

Characterizations

The X-ray powder diffraction (XRD) patterns were recorded on a Bruker D8 advanced X-Ray diffractometor with Cu Kα radiation (λ=1.54178 Å). Morphologies and structures of samples were characterized by scanning emission microscope (SEM, Hitachi X650), transmission electron microscope (TEM, JEOL JEM-1011) and HRTEM (JEOL JEM-2100). X-ray photoelectron spectroscopy (XPS, ESCALAB 250) was carried out to analyze the element and valence state in the composites. The N_2 adsorption/desorption isotherms were obtained to determine the specific surface area and pore size distribution from a Quadrasorb SI analyzer at 77 K. Thermogravimetric analysis (TGA) was recorded to measure the carbon contents on a Mettler Toledo TGA/SDTA851 thermal analyzer apparatus at a heating rate of 10°C min^{-1} in flowing air. Raman spectra was measured on a Jobin Yvon (France) LABRAM-HR confocal laser micro-Raman spectrometer at room temperature.

Electrochemical measurements

The working electrodes were fabricated by mixing the slurry of 70 wt.% active materials, 20 wt.% acetylene black (Super-P) and 10 wt.% carboxymethylcellulose sodium (CMC) in ultra-pure water. The 20 wt.% acetylene black (Super-P) was used in excess to improve electronic conductivity and obtain more excellent electrochemical performance of transition metal oxides. The resulting slurry was casted on copper foil by thickness of 300 μm scraper and dried overnight in vacuum oven at 60°C. The fabricated electrodes were calendered and cut into discs with a final thickness of 13 μm. The diameter of electrode is 12 mm with a mass loading of 1 mg cm^{-2}, and the coating density of the electrode is about 0.77 g cm^{-3}. The CR-2032-coin cells were assembled in an argon-filled glove box (water and oxygen content less than 0.5 ppm) using pure lithium foil as the counter electrode, Celgard 2300 membrane as a separator and 1 mol L^{-1} $LiPF_6$ in a mixture of ethylene carbonate (EC) and dimethyl carbonate (DMC) (volume ratio = 1:1) as the electrolyte. Cyclic voltammetry (CV) was operated between 0.05-3.0 V at a scanning rate of 0.1 mV s^{-1} on an electrochemical workstation (CHI 760C, Shanghai, China) at 30°C in the incubator. Galvanostatic discharge/charge cycles were performed in the voltage range of 0.05-3.0 V *vs.* Li^+/Li on a lithium-ion battery cycler (LAND CT-2001A, Wuhan, China) at 30°C in the incubator. Electrochemical impedance spectra (EIS) were collected from an electrochemical workstation (Materials Mates 510, Italia) in a frequency range from 0.1 MHz to 0.01 Hz.

Results and discussion

The synthesis route of porous MnO@C/CNTs is demonstrated in Fig. 1. The flowers-like $Na_{0.55}Mn_2O_4$, composed of thin and smooth nano-sheets, were synthesized by dealloying the Mn/Al alloy with the electrolyte-species-solid mechanism.[12] Subsequently, the precursors were thermally annealed in alternating atmospheres of argon, acetylene/argon (mole ratio = 5:95), and argon gas to evolve the porous MnO@C/CNTs. Apparently, upon thermal treatment, $Na_{0.55}Mn_2O_4$ nano-sheets were decomposed into MnO nanoparticles, which were surface coated with ultra-thin carbon layer to form a core-shell structure. Meanwhile, innumerable CNTs were produced simultaneously, providing a conducting network for electrochemical active MnO nanoparticles. The temperature sequences and gas conditions are crucial for morphology of modified carbon materials. This will be detailedly discussed in the following part.

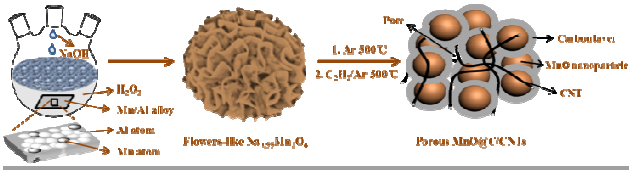

Fig. 1. Schematic illustrating of preparation process of porous MnO@C/CNTs materials.

X-ray powder diffraction (XRD) patterns were obtained to provide insight of the structural transformation process, as shown in Fig. 2. Upon dealloying, Mn/Al alloy first transformed into a monoclinic phase $Na_{0.55}Mn_2O_4$ (JCPDS No. 43-1456, Fig. 2a). The main peaks located at around 12 and 25□(2θ) are characteristic for the (001) and (002) planes. After annealing in Ar, the distinct diffraction peaks match well with tetragonal phase Mn_3O_4 (JCPDS No. 24-0734, Fig. 2b). Interestingly, upon a subsequent thermal annealing in the C_2H_2/Ar mixed gas at 500°C, the tetragonal phase Mn_3O_4 will completely transformed into pure MnO phase, which is surface decorated by ultrathin carbon layer and inter-spaced by numerous CNTs. As shown in Fig. 2c, the main diffraction peaks of sample MnO@C/CNTs architectures are in good agreement with the cubic MnO (JCPDS no. 07-0230), and no impure peaks of other Mn-based oxide are observed. The diffraction patterns for carbon materials can not be detected mainly due to the low amount.

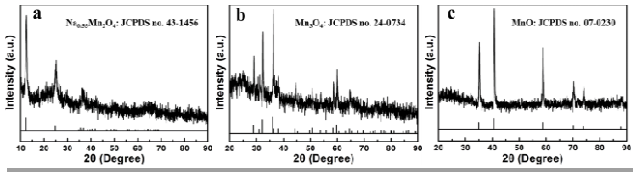

Fig. 2. (a) XRD patterns of (a) $Na_{0.55}Mn_2O_4$, (b) Mn_3O_4 and (c) MnO@C/CNTs.

The morphology evolution for the prepared products was investigated by TEM as shown in Fig. 3. $Na_{0.55}Mn_2O_4$ samples exhibit flowers-like with a diameter around 1.5 μm, composed of numerous thin nano-sheets with a relatively smooth surface (Fig. 3a). After being sintered at 500°C in Ar, the surface becomes coiling, and the intermediate products of Mn_3O_4 maintain the hierarchical flower-like structures with thicker nano-sheets than the $Na_{0.55}Mn_2O_4$ precursors (Fig. 3b). Upon further annealing in C_2H_2/Ar gas mixture, these nano-sheets are decomposed into MnO nanoparticles, which in general are still interconnected to exhibit a 3D porous architecture (Fig. 3c). The nitrogen adsorption-desorption isotherms shown in Fig. S2 feature an obvious hysteresis loop and the pore distribution curves display the porous architectures of MnO/C/CNTs composites. The specific surface area, which is about three times higher than that of previously reported,[12] reaches 18.9 m^2 g^{-1} and the average pore distribution is 78.4 nm, in good agreement with TEM observation. In addition, the Ar atmosphere pretreatment for flowers-like $Na_{0.55}Mn_2O_4$ is necessary to obtain the MnO@C architectures with both carbon

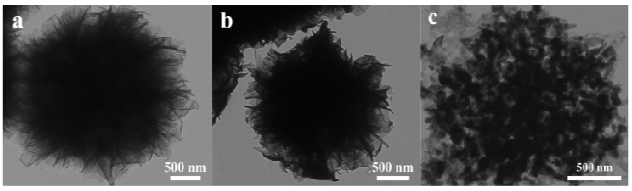

Fig. 3. TEM images of (a) flowers-like $Na_{0.55}Mn_2O_4$, (b) Mn_3O_4 and (c) porous MnO@C/CNTs.

layer and CNTs. As shown in Fig. S3&S4, CNTs could be successfully produced but the carbon layer cannot be deposited on the surface of MnO nanoparticles without Ar atmosphere pretreatment, which probably implies a stable environment for coating carbon layer on MnO active material.

The fine morphology of porous MnO@C/CNTs was further investigated by TEM and SEM. As depicted in Fig.4a, a uniform 4 nm-thick carbon coating layer is deposited on the MnO nanoparticles. As the HRTEM image shown in Fig. 4b, the distance of clear lattice fringes is 2.58 Å, which is corresponding to the (111) plane of cubic MnO, and the interface between MnO and carbon layer is clearly resolved. XPS was carried out to confirm the surface oxidation state of the porous MnO@C/CNTs. Figure. S5a shows the survey peaks of Mn (2*s*, 2*p*, 3*s*, and 3*p*) and O (1*s*), which can be assigned to MnO.[12] The high-resolution XPS peaks of Mn $2p_{1/2}$ and Mn $2p_{3/2}$ are located at 652.8 and 641.0 eV, in well accordance with MnO (Fig. S5b). Figure. 4c shows that the architectures are hierarchical aggregations with CNTs based on the existing structure heredity (as also shown in Fig. S6). According to high-magnification TEM (Fig. 4d), the inner-diameter of CNTs is around 4.8 nm. It is worth noting that the precursors hold the feature of the necessary catalytic activities for CNTs formation. The possible formation mechanism is that acetylene molecules could strongly adsorb on the surfaces of oxide precursors. At high enough temperature, these unsaturated hydrocarbon molecules decompose through a dehydrogenation process. Finally, the C_xH (polymeric carbon chains) form and turn into graphitic layer.[23, 24]

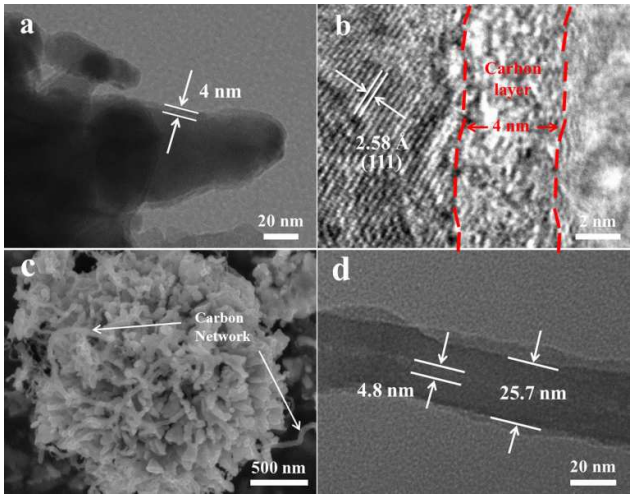

Fig. 4. (a) TEM, (b) HRTEM, and (c) SEM images of porous MnO@C/CNTs. (d) TEM image of CNTs.

Figure 5a shows the thermogravimetric analysis of porous MnO@C/CNTs composites. Because of the oxidation of MnO and the combustion of carbon layer and CNTs between 200 and 700°C, the content of carbon in the architectures is estimated to be about 19.41 wt.% based on the theoretical value (11.27 wt.%) of the weight increasing from MnO to Mn_2O_3 and the whole weight decreasing from C to CO_2.[28] Raman spectra were obtained to investigate the carbon mode as shown in Fig. 5b. The characteristic

D band (1333 cm^{-1}, graphite defects related with amorphous carbon) and G band (1591 cm^{-1}, graphite lattice attributed to sp^2 carbon atoms) are clearly observed for the architectures.[29, 30] The intensity ratio of G to D is greater than 1, indicating that graphitic domains are higher in the composites, which benefits the electron and Li^+ transport for improving electrochemical performance.[8, 31]

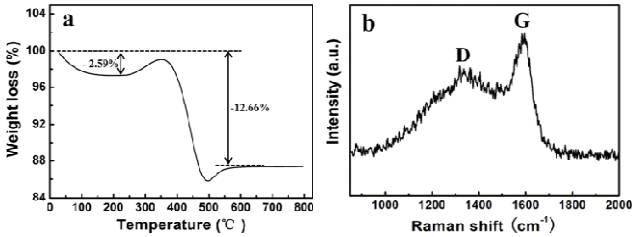

Fig. 5. TGA (a) and Raman spectrum (b) curves of porous MnO@C/CNTs.

In order to understand the redox reaction of the hybrid porous MnO@C/CNTs composites, CV curves were recorded between 0.05 and 3.0 V for the initial five cycles, as shown in Fig. 6a. In the first cathodic sweep, irreversible reduction peaks close to 1.32 and 0.1 V agree with the formation of SEI layers and the reduction of Mn^{2+} to Mn^0.[28, 32] The reduction peak shifts to 0.44 V from the second cycle onward due to the improved kinetics of formation of amorphous Li_2O and metallic manganese ($MnO + 2\ Li^+ + 2\ e^- \rightarrow Li_2O + Mn$).[12] It keeps stable from the second cycle which illustrats the enhanced reaction kinetics by double carbon modification. For the anodic process, an oxidation peak around 1.31 V appears, which can be ascribed to the oxidation of Mn^0 to Mn^{2+}.[19] In the subsequent cycles, the profiles of CV curves are overlapped well with each other, demonstrating the good reversibility during electrochemical reactions.

Figure 6b shows discharge/charge profiles at a current density of 200 mA g^{-1} within the voltage window of 0.05-3 V. In the first cycle, the discharge plateau at about 0.1 V results from the reduction of Mn^{2+} to Mn^0 and the formation of SEI layers. Subsequently, two distinct long voltage plateaus locate at around 0.45 and 1.30 V *vs.* Li/Li^+, corresponding to the reduction of Mn^{2+} to Mn^0 and the oxidation of Mn^0 to Mn^{2+}, respectively. This phenomenon is in agreement with the above CV curves. The first discharge and charge capacities of the MnO@C/CNTs electrodes are 1089 and 735 mAh g^{-1} at 200 mA g^{-1}, respectively. The irreversible capacity loss may result from the irreversible process of electrolyte decomposition and the formation of a SEI layer.[11, 32] It is comparable with other reported MnO-based electrodes. After 300 discharge/charge cycles, the hybrid MnO@C/CNTs show a high reversible capacity of 1453 mAh g^{-1} (Fig. 6c), which is much higher than the theoretical capacity of MnO (756 mAh g^{-1}) due to larger electrochemical active surface area of porous hybrid micro/nano structures and the reversible growth of a polymeric gel-like film catalyzed by 3d metals as proposed by J. M. Tarascon.[7, 9] The coulombic efficiency is nearly 100% even at the 300th cycle. The cycling volumetric capacity performance of porous MnO@C/CNTs is shown in Fig. S7. The first discharge and charge volumetric capacities of the MnO@C/CNTs electrodes are 664 and 448 mAh cm^{-3} at 200 mA g^{-1}, respectively. After 300 cycles, it still keeps a high reversible capacity of 886 mAh cm^{-3}, which is lower than that of the theoretical value of 4060 mAh cm^{-3} (the theoretical capacity of MnO is 756 mAh g^{-1} and the density is 5.37 g cm^{-3}). This is mainly due to the low tap density of the nano materials which are popular in nano materials. This highly stable performance is associated with the well reversibility of electrochemical reactions of MnO microsphere structure by carbon modification. We compared the discharge volumetric capacities of MnO@C/CNTs and commercial graphite electrodes at 200 mA g^{-1} after 20 cycles, as shown in Fig. S8. The discharge capacities of MnO@C/CNTs are higher than commercialized anode mateirals. In addition, the graphite electrode keeps a volumetric capacity of 224 mAh cm^{-3}, which is lower than that of the theoretical value of 850 mAh cm^{-3} (the theoretical capacity of graphite is 372 mAh g^{-1} and the density is 2.25 g cm^{-3}).[33] And the cycle performance has also been investigated within the voltage window of 0.05-1.5 V at a current density of 200 mA g^{-1} as shown in Fig. S9. The first discharge and charge capacities of the MnO@C/CNTs electrodes are 964 and 503 mAh g^{-1}, respectively. After 20 cycles, the architectures anodes keep a high reversible capacity of 300 mAh g^{-1}.

To better evaluate the electrochemical superiority of the porous hybrid micro/nano structures by double carbon modification, we compared the cyclic stability of MnO@C/CNTs, MnO/CNTs and Mn_3O_4 electrodes at 500 mA g^{-1}, which are presented in Fig. 7a. With the prolonged cycles, the capacity of MnO@C/CNTs electrode transition metal oxides electrodes.[19, 28, 34, 35] This rising trend may be attributed to the reconstruction of different types of electrochemically active sites in the porous MnO@C architectures.

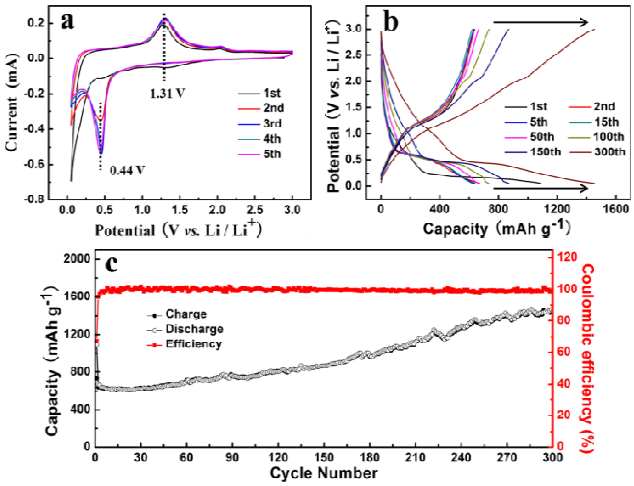

Fig. 6. (a) CV curves of porous MnO@C/CNTs at a scan rate of 0.1 mV s^{-1} in a voltage range of 0.05-3 V *vs.* Li/Li^+. Discharge/charge voltage profiles (b) and cycling performance (c) of porous MnO@C/CNTs at different cycles with a current density of 200 mA g^{-1}.

After 300 cycles, the hybrid MnO@C architectures anodes still keep a high reversible capacity of 1266 mAh g^{-1}. These are the best results compared with other reported MnO-based anodes, as summarized in Table S1. The improved cycling stability and high reversible specific capacity indicate that the porous structure

assembled by nanoparticles and hybrid of carbon layer and CNTs can buffer the huge volume change during the redox reaction, which is also confirmed by the TEM and SEM (Fig. 8). After 100 cycles, the porous micro/nano structures are absolutely retained albeit the nanoparticles become rough, demonstrating that the architectures can buffer the huge volume change. For the MnO/CNTs electrodes (without carbon core-shell structure), the capacity gradually rises to 1077 mAh g^{-1} during about 200 cycles. However, the capacity then drops to 436 mAh g^{-1} in the 300th cycle, further indicating that core-shell structures contribute to buffer the volume expansion and thus improve cycling stability. For Mn_3O_4, the discharge capacity drops quickly to 81 mAh g^{-1} after 300 cycles at the same current density. Thus, these results further demonstrate that porous structure with double carbon modification can deliver an excellent electrochemical performance.

To further explain the superior electrochemical kinetics behaviors of hybrid porous MnO@C/CNTs architectures, electrochemical impedance spectra (EIS) measurements were performed after 5 cycles at the full charge state (Fig. 7b). The similar Nyquist plots are consisted of semi-circle in the high-medium frequency region attributed to the charge transfer resistance (R_{ct}) at the electrolyte/electrode interface and a slope in the low frequency region attributed to the linear Warburg impedance (Z_w) of the diffusion of the lithium ions.[36, 37] Both the porous MnO@C/CNTs and MnO/CNTs electrodes exhibit much lower charge transfer resistances than the Mn_3O_4 electrode, indicating that carbon layer and/or CNTs are beneficial for improving the conductivity and enhancing the electrochemical dynamic behavior. From the insert in Fig. 7b, R_{ct} of MnO@C/CNTs is lower than that of MnO/CNTs, indicating that double carbon modification can further facilitate the electron/ion transport at the electrode/electrolyte interface. To further investigate the resistance evolution during cycles, Fig. S10 shows the EIS of MnO@C/CNTs electrode after 1, 15, 50, and 100 cycles at the full charge state. The Nyquist plots are similar at various cycles, and the R_{ct} gradually reduces before 50 cycles, suggesting the activation of architectures and the improved kinetics of the reaction.[28] From 50th cycles upwards, R_{ct} tends to be stabilized. These results illustrate that MnO@C/CNTs can be good candidates for LIBs anodes.

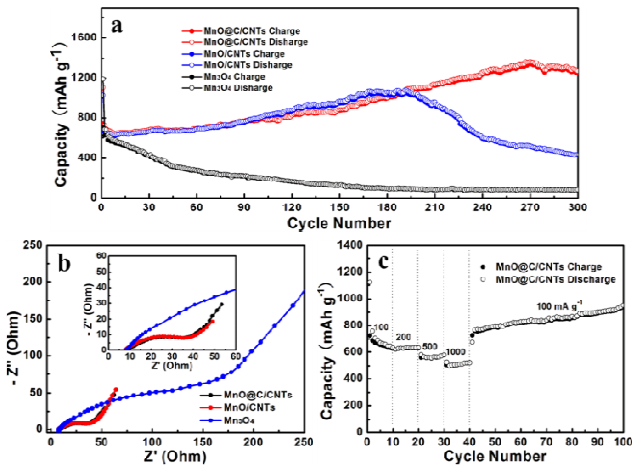

Fig. 7. (a) Cycling performance of porous MnO@C/CNTs, MnO/CNTs and Mn_3O_4 electrodes with a current density of 500 mA g^{-1}. (b) EIS of the porous MnO@C/CNTs, MnO/CNTs and Mn_3O_4 electrodes after 5 discharge/charge cycles at 500 mA g^{-1} at the full charge state. (c) Rate capabilities of porous MnO@C/CNTs electrodes at various current densities of 100, 200, 500, 1000 mA g^{-1}.

Rate capability of MnO@C/CNTs electrode was investigated at discharge/charge current densities range from 100 to 1000 mA g^{-1} as shown in Fig. 7c. Even at the current density of 1000 mA g^{-1}, the discharge capacity of MnO@C architectures is 422 mAh g^{-1}, much higher than the theoretical value of graphite (372 mAh g^{-1}). When the current density returned to 100 mA g^{-1}, a high reversible discharge capacity of 850 mAh g^{-1} can be retained after total 100 cycles, indicating good structural stability and low kinetic-limited of the hybrid porous MnO@C architectures.

The excellent electrochemical properties of MnO@C/CNTs electrode could be assigned to the integration of porous structure, nanoscale size along with the hybrid of carbon layer and CNTs doping, all of which have been reported to be efficient strategies to improve the lithium-storage performance. The porous structure and MnO@C core-shell structure could tolerate the volume changes during cycling. Also, CNTs could increase the contact among active particles and electrolyte and improve the reaction kinetics. In addition, the nanoscale size would efficiently shorten the electron and lithium ion diffusion pathway and reduce volume fluctuation.

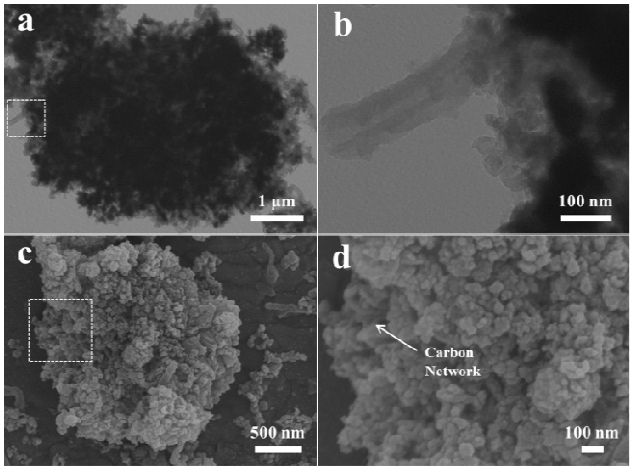

Fig. 8. (a, b) TEM and (c, d) SEM of porous MnO@C/CNTs electrodes after 100 cycles at 500 mA g^{-1}.

Conclusions

In summary, we have successfully developed a modified dealloying technology and a CCVD method for in-situ fabrication of porous MnO@C/CNTs material (carbon layer, 4 nm in thickness, CNTs, 4.8 nm in inner-diameter). The procedure taken for thermal annealing was found to be highly crucial for the successful fabrication of desired nanocomposites. When employed as anodes of LIBs, the porous MnO@C/CNTs electrodes exhibit promising high

discharge capacity (1266 mAh g^{-1} at 500 mA g^{-1} after 300 discharge/charge cycles) and excellent capacity retention (850 mAh g^{-1} at 100 mA g^{-1} after 100 rate cycles). Overall, porous MnO@C/CNTs can be applied as a new anode material for the next generation energy technologies with superior electrochemical performance.

Acknowledgements

This work was supported by the National 973 Program Project of China (2012CB932800), the National Science Foundation of China (51171092, 21203111). Y. D. also acknowledges the Natural Science Foundation of Tianjin and the Fundamental Research Funds of Shandong University.

References

1 X.J. Feng, J. Yang, Y.T. Bie, J.L. Wang, Y.N. Nuli and W. Lu, *Nanoscale,* 2014, **6**, 12532-12539.
2 M.V. Reddy, G.V.S. Rao and B.V.R. Chowdari, *Chem. Rev*., 2013, **113**, 5364-5457.
3 S.H. Choi, Y.N. Ko, K.Y. Jung and Y.C. Kang, *Chem-Eur. J*., 2014, **20**, 11078-11083.
4 X.Y. Lai, J.E. Halpert and D. Wang, *Energy Environ. S*ci., 2012, **5**, 5604-5618.
5 G.N. Zhu, H.J. Liu, J.H. Zhuang, C.X. Wang, Y.G. Wang and Y.Y. Xia, *Energy Environ. S*ci., 2011, **4**, 4016-4022.
6 S.L. Jin, H.G. Deng, D.H. Long, X.J. Liu, L. Zhan, X.Y. Liang, W.M. Qiao and L.C. Ling, *J. Power Sources,* 2011, **196**, 3887-3893.
7 P. Poizot, S. Laruelle, S. Grugeon, L. Dupont and J.M. Tarascon, *Nature,* 2000, **407**, 496-499.
8 H. Jiang, Y.J. Hu, S.J. Guo, C.Y. Yan, P.S. Lee and C.Z. Li, *ACS Nano,* 2014, **8**, 6038-6046.
9 S.M. Guo, G.X. Lu, S. Qiu, J.R. Liu, X.Z. Wang, C.Z. He, H.G. Wei, X.R. Yan and Z.H. Guo, *Nano Energy,* 2014, **9**, 41-49.
10 Y.Y. Wang, X.J. Jiang, L.S. Yang, N. Jia and Y. Ding, *ACS Appl. Mater. Inter.,* 2014, **6**, 1525-1532.
11 Y. Xia, Z. Xiao, X. Dou, H. Huang, X.H. Lu, R.J. Yan, Y.P. Gan, W.J. Zhu, J.P. Tu, W.K. Zhang and X.Y. Tao, *ACS Nano,* 2013, **7**, 7083-7092.
12 X.J. Jiang, Y.Y. W, L.S. Yang, D.W. Li, H.Y. Xu and Y. Ding, *J. Power Sources,* 2015, **274**, 862-868.
13 G.Y. Huang, S.M. Xu, Z.H. Xu, H.Y. Sun and L.Y. Li, *ACS Appl. Mater. Inter.,* 2014, **6**, 21325-21334.
14 W.M. Zhang, X.L. Wu, J.S. Hu, Y.G. Guo and L.J. Wan, *Adv. Funct. Mater.* 2008, **24,** 3941-3946.
15 X. Zhu, Y. Zhu, S. Murali, M.D. Stollers and R.S. Ruoff, *ACS Nano,* 2011, **5**, 3333-3338.
16 Z.S. Wu, W.C. Ren, L. Wen, L.B. Gao, J.P. Zhao, Z.P. Chen, G.M. Zhou, F. Li and H.M. Cheng, *ACS Nano,* 2010, **4**, 3187-3194.
17 X.F. Sun, Y.L. Xu, P. Ding, M.R. Jia, and G. Ceder, *J. Power Sources,* 2013, **244**, 690-694.
18 S. Xin, Y.G. Guo and L.J. Wan, *Acc. Chem. Res.* 2012, **10**, 1759-1769.
19 X.W. Li, S.L. Xiong, J.F. Li, X. Liang, J.Z. Wang, J. Bai and Y.T. Qian, *Chem-Eur. J.,* 2013, **19**, 11310-11319.
20 B. Sun, Z.X. Chen, H.S. Kim, H. Ahn and G.X. Wang, *J. Power Sources,* 2011, **196**, 3346-3349.
21 S. Zhang, L.X. Zhu, H.H. Song, X.H. Chen and J.S. Zhou, *Nano Energy,* 2014, **10**, 172-180.
22 X.F. Sun, Y.L. Xu, P. Ding, G.G. Chen, X.Y. Zheng, R. Zhang and L. Li, *J. Power Sources,* 2014, **255**, 163-169.
23 H. Wang, Y. Yuan, L. Wei, K.L. Goh, D.S. Yu and Y. Chen, *Carbon,* 2015, **81**, 1-19.
24 V. Jourdain and C. Bichara, *Carbon,* 2013, **58**, 2-39.
25 Y. Ding and M.W. Chen, *MRS Bull.,* 2009, **34**, 569-576.
26 Y.Y. Li and Y. Ding, *J. Phys. Chem. C,* 2010, **7**, 3175-3179.
27 C.X. Xu, R.Y. Wang, Y. Zhang and Y. Ding, *Nanoscale,* 2010, **2**, 906-909.
28 Y.M. Sun, X.L, Hu, W. Luo, F.F. Xia and Y.H. Huang, *Adv. Funct. Mater.,* 2013, **23**, 2436-2444.
29 W. Luo, X.L. Hu, Y.M. Sun and Y.H. Huang, *ACS Appl. Mater. Inter.,* 2013, **5**, 1997-2003.
30 F. Tuinstra and J. L. Koenig, *J.Chem. Phys.,* 1970, **53**, 1126-1130.
31 C.D.L. Casas and W.Z. Li, *J. Power Sources,* 2012, **208**, 74-85.
32 J. Yue, X. Gu, L. Chen, N.N. Wang, X.L. Jiang, H.Y. Xu, J. Yang and Y.T. Qian, *J. Mater. Chem. A,* 2014, **2**, 17421-17426.
33 O. Mao, R. L. Turner, I. A. Courtney, B. D. Fredericksen, M. I. Buckett, L. J. Krause, and J. R. Dahn, *Electrochem. Solid-State Lett.*, 1999, **2**, 3-5.
34 G.M. Zhou, D.W. Wang, F. Li, L.L. Zhang, N. Li, Z.S. Wu, L. Wen, G.Q. Lu and H.M. Cheng, *Chem. Mater.,* 2010, **22**, 5306-5313.
35 Q. Hao, J.P. Wang and C.X. Xu, *J. Mater. Chem. A,* 2014, **2**, 87-93.
36 J. Zang, H. Qian, Z.K. Wei, Y. Cao, M.S. Zheng and Q.F. Dong, *Electrochim. Acta,* 2014, **118**, 112-117.
37 F. Ciucci and W. Lai, *Electrochim. Acta,* 2012, **81**, 205-216.
38 J. Mai, D. Zhang, Y.Q. Qiao, C.D. Gu, X.L. Wang and J.P. Tu, *J. Power Sources,* 2012, **216**, 201-207.
39 S.B. Wang, Y.B. Ren, G.R. Liu, Y.L. Xing and S.C. Zhang, *Nanoscale,* 2014, **6**, 3508-3512.